MICROROBOTS

Microscopic robots with onboard digital control

Michael F. Reynolds[1], Alejandro J. Cortese[1,2], Qingkun Liu[1], Zhangqi Zheng[1], Wei Wang[1,3], Samantha L. Norris[1], Sunwoo Lee[2], Marc Z. Miskin[4], Alyosha C. Molnar[2,5]*, Itai Cohen[1,5]*, Paul L. McEuen[1,5]*

Autonomous robots—systems where mechanical actuators are guided through a series of states by information processing units to perform a predesigned function—are expected to revolutionize everything from health care to transportation. Microscopic robots are poised for a similar revolution in fields from medicine to environmental remediation. A key hurdle to developing these microscopic robots is the integration of information systems, particularly electronics fabricated at commercial foundries, with microactuators. Here, we develop such an integration process and build microscopic robots controlled by onboard complementary metal oxide semiconductor electronics. The resulting autonomous, untethered robots are 100 to 250 micrometers in size, are powered by light, and walk at speeds greater than 10 micrometers per second. In addition, we demonstrate a microscopic robot that can respond to an optical command. This work paves the way for ubiquitous autonomous microscopic robots that perform complex functions, respond to their environments, and communicate with the outside world.

INTRODUCTION

Researchers in the field of microrobotics have created an impressive variety of actuating systems, including magnetic (1–4), chemical (5–14), biohybrid (15, 16), and ultrasound (17, 18) microrobots with useful properties such as phototaxis (19–21), chemotaxis (22, 23), and magnetic control of motion direction (2, 13, 24). Most existing microrobotic systems achieve simple motion in the presence of an external power source, but a few recent examples have demonstrated actuation through a series of states to form a gait using either light (12, 25) or magnetic fields (3, 26, 27). For example, prior work within our group developed microscopic robots that combine surface electrochemical actuators (SEAs) and silicon photovoltaics (PVs) as a proof of concept for microrobots with silicon electronics (25). However, even these robots are only "marionettes" (28), requiring an external user to control the actuation of each leg. Existing microscopic robots, therefore, achieve certain simple criteria for autonomy, such as onboard power and some sensing capabilities, but lack onboard control, a key metric for autonomy in small robots (29). As noted in numerous reviews, making microscopic robots that respond to internal information processing instead of external controls would set the stage for "next-generation intelligent micromachines that can adapt to diverse scenarios for use in emerging fields" (28, 30–32). Building these systems around complementary metal oxide semiconductor (CMOS) microelectronics is a particularly appealing approach because it would allow researchers to leverage decades of work on microelectronic circuits and sensors to give microrobots complex functions (33). Previous work to miniaturize robots with onboard CMOS electronics has demonstrated untethered robots just under 10 mm in size (34–37, 29). However,

the techniques used to build these robots—including wire bonding and multichip stacking—prevent them from shrinking to even smaller sizes. Building untethered microscopic robots controlled by integrated circuits (ICs) is therefore a major unsolved technology integration challenge (31, 32, 34), requiring complex fabrication processes for integrating microelectronics for information processing, onboard energy harvesting, and electrically addressable microactuators to complete autonomous microscopic robots.

RESULTS

Here, we show how to overcome these challenges and demonstrate microscopic robots controlled by onboard digital circuitry, described in Movie 1. These robots are about 10,000 times smaller by volume than previously demonstrated robots with onboard CMOS electronics. Figure 1A shows one such microscopic robot pictured next to an ant. The robot cannot be resolved by the naked eye, appearing only as a bright speck when it scatters light. In Fig. 1B, we zoom in on the robot. The robot contains an application-specific IC (ASIC), which consists of ~1000 transistors in addition to diodes, resistors, and capacitors, and generates a clock signal that is used to produce a series of phase-shifted square waves for setting the gait of the robots. In addition to the CMOS circuitry, it has silicon PVs that, when exposed to light, power the robot. It also has legs made of SEAs (25) and rigid silicon dioxide panels (Fig. 1C) (38). The SEAs consist of an ultrathin layer of platinum (~7 nm) and a capping layer of titanium (~2 nm). When the actuator receives a voltage signal from the CMOS circuit, oxygen adsorbs at and expands the platinum surface, causing the robot leg to bend. These actuators are capable of lifting and moving the robot despite being about 1000 times thinner than the robot's body.

The key difference between this robot and previously reported microscopic machines is the onboard ASIC. Figure 1D shows the computer-aided design (CAD) layout of the IC that controls the robot, fabricated by X-FAB Silicon Foundries in their 180-nm CMOS silicon-on-insulator process. It consists of a well-defined current reference, relaxation oscillator (39, 40), frequency divider,

[1]Laboratory of Atomic and Solid-State Physics, Cornell University, Ithaca, NY, USA. [2]Department of Electrical and Computer Engineering, Cornell University, Ithaca, NY, USA. [3]Sibley School of Mechanical and Aerospace Engineering, Cornell University, Ithaca, NY, USA. [4]Department of Electrical and Systems Engineering, University of Pennsylvania, Philadelphia, PA, USA. [5]Kavli Institute at Cornell for Nanoscale Science, Cornell University, Ithaca, NY, USA.
*Corresponding author. Email: plm23@cornell.edu (P.L.M.); itai.cohen@cornell.edu (I.C.); am699@cornell.edu (A.C.M.)
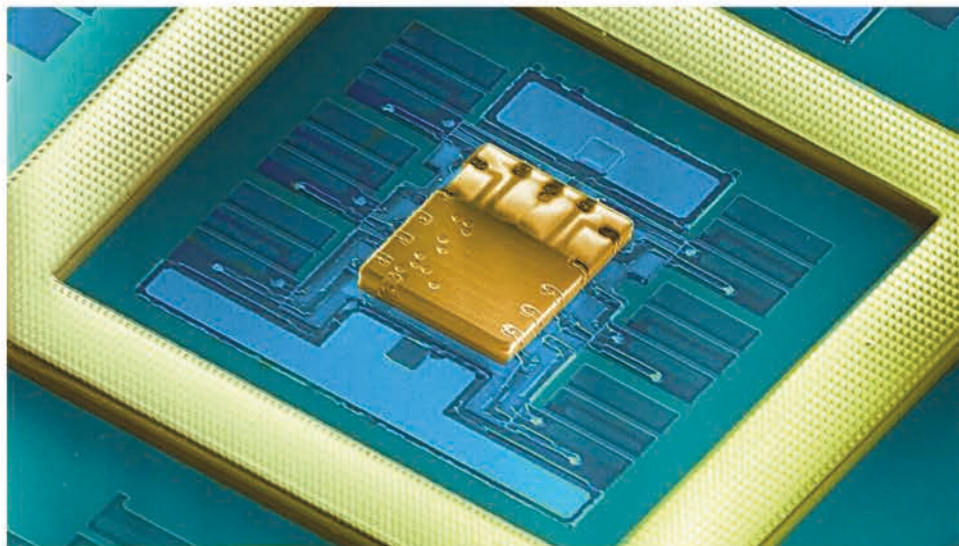
Movie 1. Overview of microscopic robots with onboard digital control.

phase shifter, and driver that together operate at <1 µW of power from the PVs (*39–41*). Details of the design of this circuit are given in Materials and Methods, and a block diagram of the components for this circuit is shown in fig. S1. Figure 1E shows an optical micrograph of the circuit only 94 µm by 55 µm in size. The large pair of PVs powers the legs of the robot; the small pair powers the circuit. The eight outputs labeled in Fig. 1E correspond to eight phase-shifted square waves (Fig. 1E, top right) that go between ±0.6 V, sufficient to drive oxygen adsorption and desorption for the SEAs driving each leg. The circuit has four redundant sets of these eight outputs to make routing interconnects between the outputs and legs easier. Multiple actuators can be connected to a single output to make legs that move simultaneously. Last, the circuits are designed so that the frequency of the square wave outputs can be set after fabrication by hard-wiring the I-shaped pins to the bar above them (Fig. 1E, bottom right). Our initial proof-of-concept robots are set to operate at about 1 to 2 Hz to make the robots less susceptible to slipping on flat surfaces. On-chip testing of these circuits demonstrates that they behave as designed, delivering square waves with a 0.6-V amplitude, currents that correspond to a PV responsivity of about 0.3 A/W, and square wave frequencies that match the designed values for about 1 kW/m^2 of illumination (~1 sun) with a frequency that increases with light intensity (Materials and Methods and fig. S2). This circuit serves as a platform around which we build a variety of robots.

The next major challenge is the heterogeneous integration of CMOS electronics and microactuators to turn these circuits into fully functioning, releasable microscopic robots. The process that we developed (a simplified version of which is shown in Fig. 2) includes 13 layers of photolithography, 12 etches, and 11 depositions involving 10 different materials at the Cornell Nanofabrication Facility. Starting from CMOS electronics received from X-FAB (Fig. 2A), we first etch around the circuit of the robot (Fig. 2B), then deposit interconnects (Fig. 2C), deposit metal to shield the circuit from light (Fig. 2D), and lastly pattern the actuators and rigid panels to make the legs (Fig. 2E). Once the robots are completed, we etch the silicon substrate beneath them and release them into

aqueous solution (Fig. 2F), typically phosphate-buffered saline (pH 7.5). After releasing the robots, we can manipulate them individually with micropipettes (movie S1). The complete fabrication recipe can be found in the Supplementary Materials and fig. S3. The overall yield of working robots is about 50%; yield-limiting steps and future techniques for improving them are also discussed in the Supplementary Materials. All of the processes are modular and parallel, producing hundreds of copies of multiple robot designs from an area less than 50 mm^2. These can be adapted and expanded in the future to create new generations of autonomous microscopic robots with ever-more sophisticated functions using the same design tools for creating semiconductor ICs.

A simple two-legged autonomous microscopic robot walking independently across a smooth silicon wafer is shown in Fig. 3A and Movie 2 (with details for operation of the robots in Materials and Methods). For this robot (and all other robots shown afterward), the legs can move independently of each other by applying potentials versus large platinum ground electrodes also exposed to the solution, as labeled in Fig. 3A. Although this robot crawls rather than swims, its design and gait are inspired by E. Purcell's three-link swimmer (*42*) that can move at low Reynolds number by breaking time reversal symmetry. We therefore call this robot "Purcell-bot." The distance traveled by Purcell-bot versus time (measured by tracking the robot center) is plotted in Fig. 3B. The Purcell-bot shown here moves at a speed of about 4 to 5 µm/s, about two body lengths per minute. The circuit is set so that this robot performs one complete gait cycle at a frequency of about 1 Hz when powered by less than 1 kW/m^2 of light intensity. The distance traveled over one cycle is ~4 µm (inset of Fig. 3B).

The distance traveled per cycle in Fig. 3B can be explained with a simple proposed model based on the change in frictional forces on the legs as a function of their position. Figure 3C shows side-view schematics and top-down microscope images for each step in one full cycle of Purcell-bot's gait with labels corresponding to the inset of Fig. 3B. Starting from a position where both legs are extended (0), the legs alternately bend inward toward the robot's body (1 and 2), and then outward, back to their starting positions (3 and 4). The
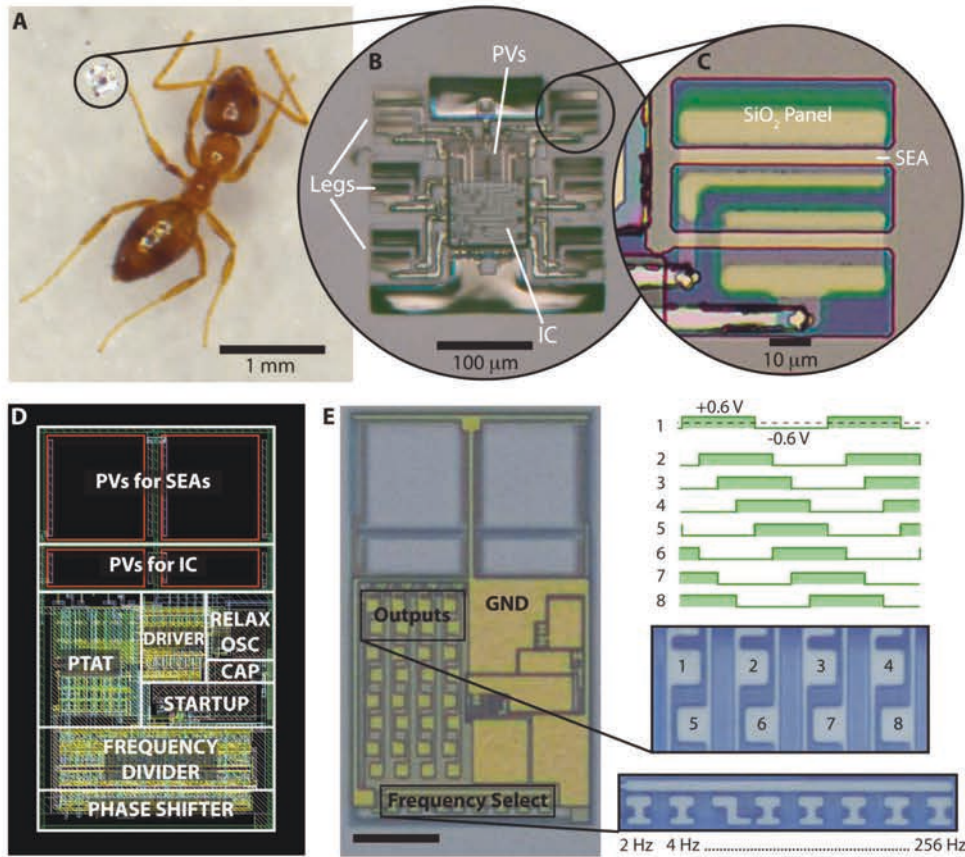
Fig. 1. Autonomous microscopic robots. (**A**) A microscopic robot next to an ant. (**B**) A zoomed-in view of the robot. The robot is composed of three primary pieces: an IC for controlling the robot, legs to allow the robot to walk, and PVs for powering both the legs and the circuit. (**C**) Further zoomed-in image showing one leg of the robot. It consists of rigid panels of SiO_2 and SEAs, active hinges that provide the motion. (**D**) Image of the CAD layout for the circuit with the primary circuit blocks labeled. (**E**) Optical microscope image of the control circuit for the microscopic robots. Scale bar, 20 μm. The circuit has eight outputs that deliver phase-shifted square waves with a voltage amplitude of about 0.6 V. The frequency of these square waves can be set by hard-wiring the circuit's "frequency select." PTAT, proportional to absolute temperature.

robot moves a larger distance forward in (1) and (4) and a smaller distance backward in (2) and (3). We explain this behavior by noting that more weight is placed on the leg that is closest to the robot's center of mass, increasing the friction on that leg. The friction is therefore higher on the actuated leg in (1) and (4), allowing that leg to pull or push the robot forward, whereas the friction is higher on the static leg in (2) and (3), allowing the actuated leg to slide while moving the robot backward a smaller distance. If the leg with higher friction remained completely fixed, Purcell-bot could move a distance of $2d_{leg}$ per cycle—about 20 μm for the robot shown in Fig. 2—where d_{leg} is the distance each leg moves along the surface during actuation. In practice, this robot travels about 20% of the maximum distance because both legs slide somewhat during each step of the motion. This accounts for the backward motion during steps 2 and 3 of the robot's motion shown in the inset of Fig. 3B. This model also indicates that the speed of motion will be highly sensitive to local changes in friction, a possible explanation for the change in average speed during the measurement. In the future, therefore, increasing the friction between the legs and surface, the length and design of the legs, and the frequency of actuation could result in faster speeds even for this simple robot, as discussed in Materials and Methods. Purcell-bot's behavior

matches qualitatively with that of macroscopic crawling robots designed with the same gait, an example of which is shown in fig. S4.

The circuit can also drive more complicated legged locomotion. Figure 4 shows "antbot," a hexapod robot inspired by the motion of ants. Images of antbot crawling on a glass coverslip are shown in Fig. 4A and Movie 3. The displacement of the robot versus time is plotted in Fig. 4B; antbot moves at a consistent average speed of about 12 μm/s, about three body lengths per minute. The instantaneous speed can be greater than 50 μm/s, as shown in Fig. 4C. On the basis of the size and weight of the robot, the drag coefficient, and this peak speed, the legs exert a peak force of about 1 nN to move the robot forward, close to the previously measured maximum force output of a square SEA (25). The frequency of the gait is about 2.5 Hz, so the robot moves about 5 μm per stride. Antbot moves with a gait common to many insects called an alternating tripod gait (43, 44). In this gait, the top and bottom legs on one side of the robot move synchronously with the middle leg on the other side of the robot and are out of phase with the other three legs, as indicated by the labels in Fig. 4D. For this robot, the hinges on the legs labeled "1" are wired to outputs 3 and 1, and the hinges on the legs labeled "2" are wired to outputs 5 and 7. This gait allows the robot to balance on three legs at a time and push off with those
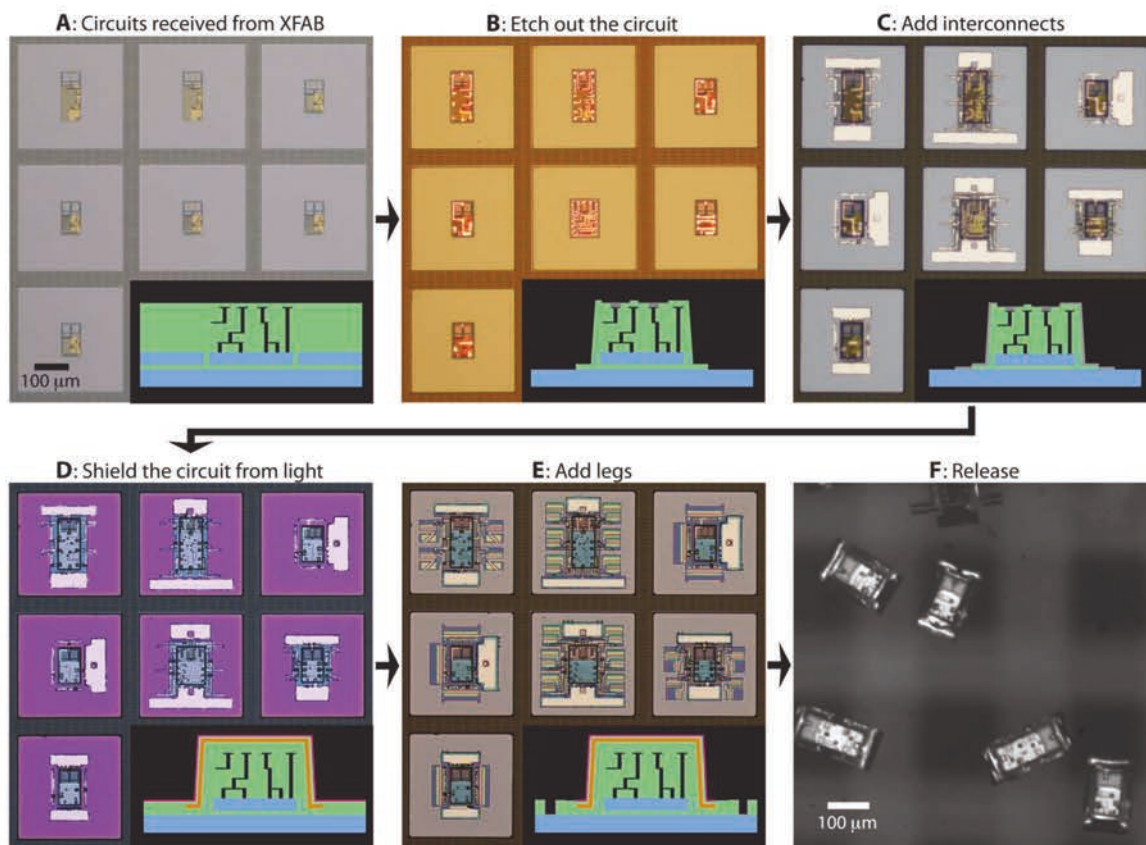
Fig. 2. Simplified fabrication process. Optical micrographs show different steps along the fabrication process, with a schematic cross section in the bottom right corner. (**A**) ICs as received from X-FAB. (**B**) Wire up the top of the circuit and etch out the circuit body. (**C**) Deposit interconnects from the circuit to the bottom silicon. (**D**) Add metal shielding to protect the circuit from light. (**E**) Etch out the panels that form the hinges of the legs and deposit SEAs. (**F**) Undercut the bottom silicon and release the robots into aqueous solution.

legs to move forward while avoiding drag from the other legs. Figure 4E tracks the motion of one leg on each phase (indicated by the boxed numbers in Fig. 4D) with respect to the body, showing an about 90° phase difference between the two (with some additional fluctuations within each cycle). Despite these fluctuations, which could be caused by microscale debris visible around the robot, the antbot's average speed remains about constant in time. We watched this particular robot for more than 15 min, during which it completed more than 2000 cycles of its gait.

Building microscopic robots with CMOS electronics also allows us to create robots that change their behavior in response to external stimuli. To demonstrate this capability, we built "dogbot," which responds to a simple command (Fig. 5). In this case, the command is delivered optically and tells the robot to speed up (Movie 4). To communicate with dogbot, we modulate the full-field intensity of light incident on the robot, as shown schematically in Fig. 5A. We designed dogbot's circuit to receive Manchester-encoded commands, a standard communication protocol where bits are encoded in transitions from high to low or low to high instead of in the levels themselves, allowing data and timing information to be transmitted to the robot within a single optical signal (*45, 46*). A block diagram for this circuit is shown in fig. S5. The additional circuitry for dogbot expands its area to be about 50% bigger with about 1500 transistors. Figure 5B shows the CAD layout for

dogbot's circuit. In addition to the previous circuit components, dogbot has an optical receiver, Manchester decoder, and command checker. The optical receiver contains another PV, the output of which is fed to the Manchester decoder. The Manchester decoder interprets the incident signal to retrieve a four-bit binary word, which it compares with a known four-bit code. If the received binary word matches the known code, the frequency of the outputs to the legs increases by a factor of 2. On-chip testing of this circuit is shown in fig. S6. Although we designed the circuit to receive only one command, this scheme for communication with microscopic robots is scalable. The area of the robot scales linearly with the number of bits, whereas the number of commands scales exponentially; an eight-bit dogbot could have more than 200 different commands with only a 20% increase in size. Last, we show an optical microscope image of the fully integrated dogbot in Fig. 5C.

In Fig. 5D, we show dogbot's response to a shift command that changes the gait frequency by plotting its displacement versus time (also shown in Movie 4). The robot is designed to walk with the same gait as Purcell-bot, alternately moving the legs on either side of its body. We expect its speed to increase proportionally with frequency. The robot is powered with a continuous illumination of about 1 kW/m²; to send a command, we briefly alternate the light intensity between about 1 and about 3 kW/m². The command itself is shown in the inset of Fig. 5D. In addition to the four bits for
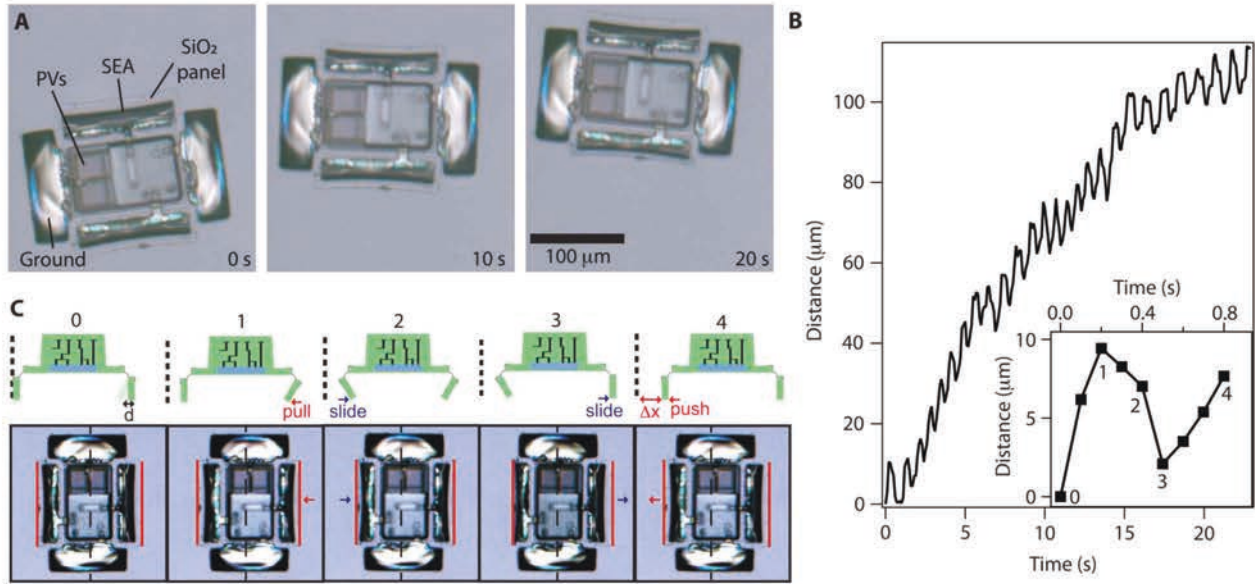
Fig. 3. Purcell-bot. (**A**) Time-lapse micrographs of a two-legged Purcell-bot walking along a silicon surface. (**B**) Distance versus time for the Purcell-bot shown in (A). Inset: Distance versus time over one cycle of the Purcell-bot's gait. (**C**) Schematic and microscope images showing the sequence of motions in one cycle of the Purcell-bot's gait, with numbers corresponding to the points in time labeled in the inset of (B). Arrows indicate the direction of motion of the legs. The lines of contact between the robot's legs and the surface are artificially highlighted with red lines to make the alternating motion easier to see.
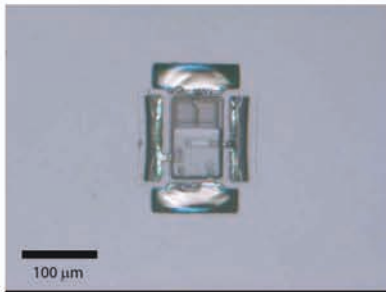
Movie 2. Purcell-bot. Real-time optical reflection microscope video of Purcell-bot crawling on a flat silicon.
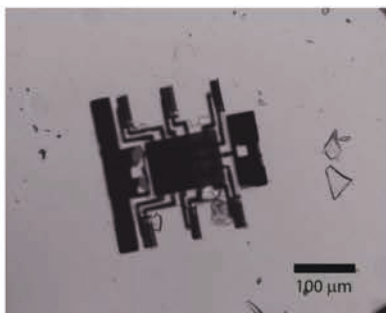
Movie 3. Antbot. Real-time optical transmission microscope video of antbot walking on a glass coverslip.

the command, it includes an initial timing sequence of ones and zeroes, which is required for the circuit to lock on to the timing to receive the command. The pulse width in the command is 50 μs—a time scale specified by the design of the circuit—so the whole command takes less than 2 ms to deliver. When dogbot receives the command, the frequency of its gait shifts from about 2 to about 4 Hz, increasing its speed from about 2 to about 6 μm/s. Although more than a factor of 2, this increase is qualitatively consistent with the expected behavior given the variability in crawling speed for the fixed-frequency Purcell-bot.

DISCUSSION

Collectively, the work shown here is the start of a new "family" of microscopic robots with numerous circuit design "genera" and locomotory strategy "species." Movies S2 and S3, for example, show two additional crawling robots with different leg designs and gaits. Because these microscopic robots are patterned in parallel using photolithography, we can build many robots and try many different designs at once. More than 300,000 of these robots could fit on a single 200-mm wafer. Future research could study and optimize the gaits of microscopic robots and build on existing literature studying microrobot locomotion (47–50). The robots that we have demonstrated thus far are still relatively simple, moving with fixed gaits in well-controlled environments and not capable of navigating rough terrain or swimming through viscoelastic media. However, because the circuits are foundry based and because the integration process has now been developed, the stage is set for other researchers to add new actuators and propulsion mechanisms as well as their own "apps"—onboard memory, chemical detectors, electromagnetic antennal arrays, etc.—to the CMOS electronics of microscopic robots. Future work on microscopic robotics can therefore expand this family tree, increasing the complexity and efficiency of the designs we presented and opening new working environments. Our group, for instance, is currently working on microactuators with higher forces and efficiencies and on robots with PV "eyes" to allow them to steer by sensing light gradients, but any
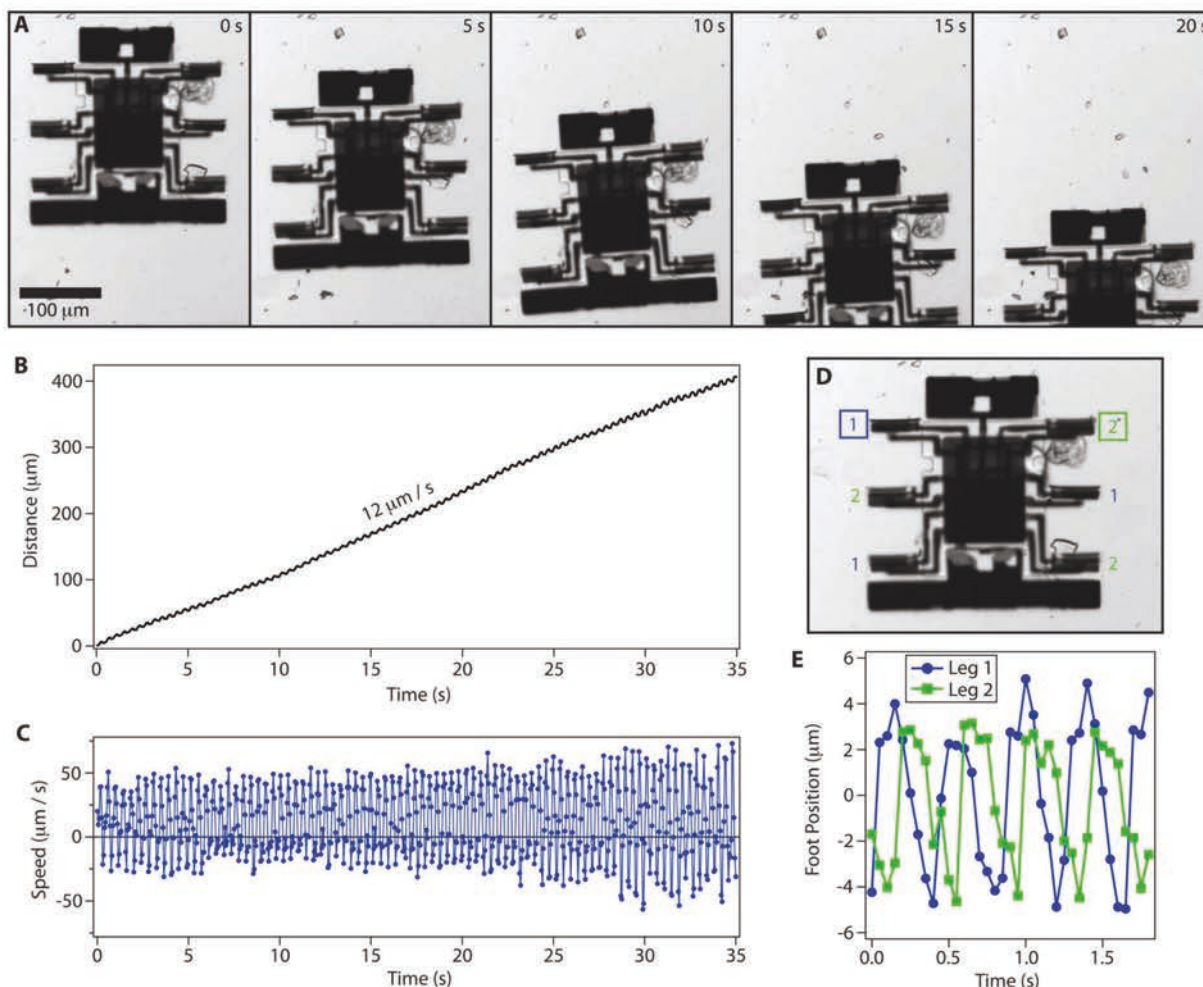
Fig. 4. Antbot. (**A**) Time-lapse microscope images of a microscopic antbot, a six-legged microscopic robot. (**B**) Distance versus time for the robot shown in (A). The antbot moves at a speed of about 12 μm/s. (**C**) Instantaneous speed of the antbot, showing maximum speeds greater than 50 μm/s. (**D**) An image of antbot with the legs labeled corresponding to their phase. Antbot moves in the same way as biological ants, using an alternating tripod gait. (**E**) Foot position for the legs indicated with squares in (D) relative to the body of the robot versus time for one leg on each of the phases, showing the phase delay between the legs.

number of microsensors and actuators could be added to give new functions to these microscopic robots. Moreover, the CMOS fabrication could, in principle, use modern node sizes of around 10 nm, enabling autonomous microscopic robots that are an order of magnitude smaller than the ones shown here. Applications would range from environmental cleanup (*24, 51*) and monitoring (*52*) to targeted delivery of drugs (*7, 53, 54*), monitoring or stimulation of cells (*55*), and microscopic surgery (*55, 56*). In all of these applications, robots with onboard control systems for sensing and responding to their environments and operating autonomously provide a notable advantage, setting the stage for ubiquitous smart microscopic robots with the capacity for positive outcomes in the world around us.

MATERIALS AND METHODS

The work reported here proceeded from circuit design and testing to fabrication to testing the completed robots, corresponding to the following Materials and Methods subsections. We also discuss how

we estimated the maximum speed and actual efficiency of these robots.

Circuit design

All circuits shown in this paper were designed in Cadence using a process design kit provided by X-FAB Silicon Foundries for their 180-nm node process, XT018. The circuit for driving the robots in Figs. 3 and 4 consisted of the circuit blocks labeled on the circuit CAD layout and in a block diagram in fig. S1 (A and B), respectively. The PVs for IC powered the proportional to absolute temperature current source, supplying a constant current to a relaxation oscillator that provided the circuit with a series of short, high-frequency pulses at ~32 kHz to serve as a clock output, a design based on prior work (*39, 40*). We then used a frequency divider that consists of a series of D-type flip-flops to convert the pulses to a 50% duty-cycle signal and to decrease that clock frequency to a range usable for the robot. We set the exact number of times that the frequency is divided when we wired up the frequency selector. The phase shifter offset the square waves controlling each output by
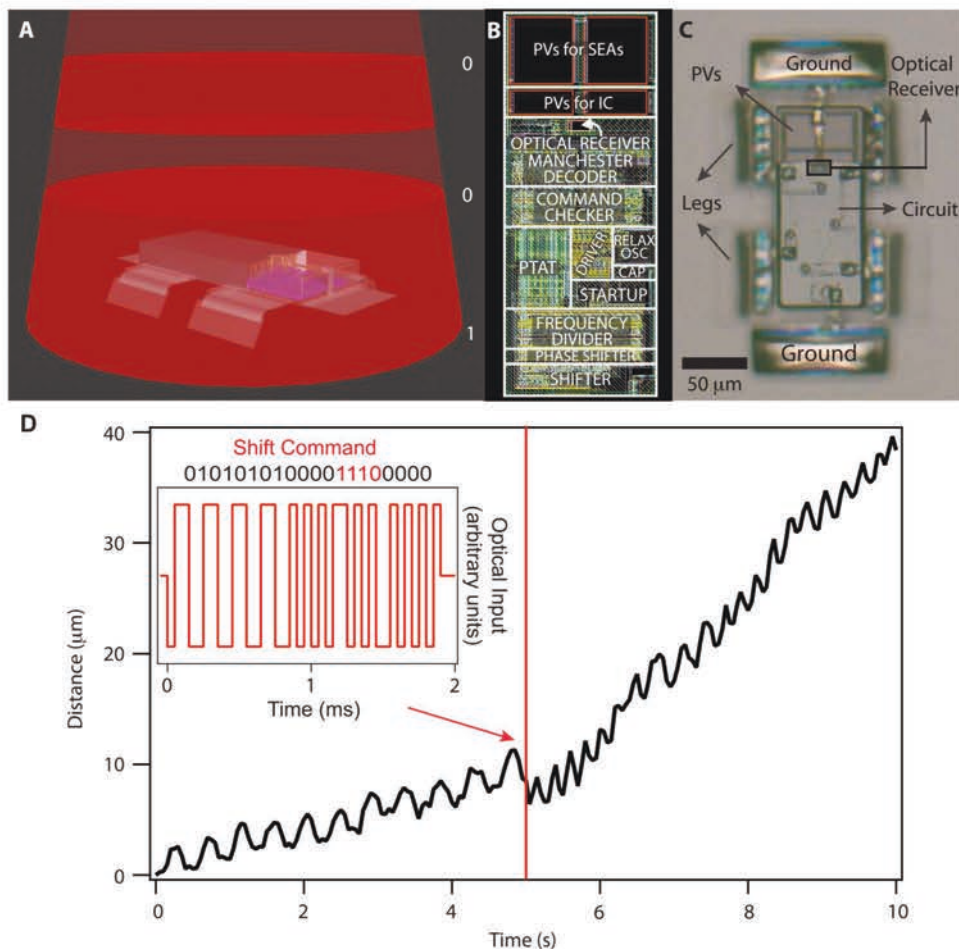
Fig. 5. Dogbot. (**A**) Schematic showing communication with dogbot. Manchester-encoded signals are given to dogbot by varying the full-field light intensity. (**B**) Image of CAD layout for dogbot. In addition to the components for the previous robots, dogbot has an optical receiver that allows it to receive commands. (**C**) Optical micrograph of fully fabricated and released dogbot. (**D**) Dogbot's distance versus time. At 5 s, dogbot receives a shift command (shown in the inset), and the frequency of motion of its legs increases by a factor of 2.
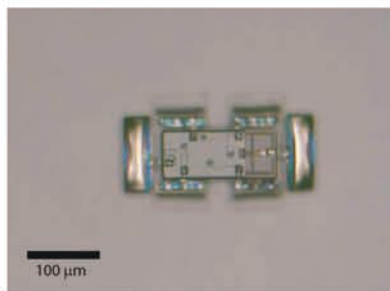
Movie 4. Dogbot. Real-time optical reflection microscope video of dogbot walking. Midway through the video, as indicated by the text on screen, dogbot receives a shift command and increases the frequency of its leg motion by a factor of 2.

multiples of one-eighth of a period, producing the phase-shifted square waves. These output signals controlled the driver for the legs, which switches from applying positive to negative voltages to the SEAs.

The circuit for dogbot, the robot shown in Fig. 5, was based on the previous circuit and was modified to allow it to respond to optical commands. The CAD layout and block diagram for this circuit are shown in fig. S5 (A and B). The added components were an optical receiver, Manchester decoder, command checker, and shifter. The optical receiver PV was connected to the Manchester decoder. The Manchester decoder interpreted the received signal to retrieve a four-bit binary word that it compared with a known four-bit code, arbitrarily chosen to be 1110 for these circuits. It was designed to receive signals with a pulse width of about 50 µs. If the received binary word matched the known code, the frequency of the outputs to the legs increased by a factor of 2, a function performed by the shifter.

Circuit testing

We tested the circuits in the laboratory by wiring up the frequency select, connecting to the output states and ground, and shielding the circuit from light with a metal layer. If the circuit was exposed to light, photocurrents at p-n junctions in the silicon caused the circuit to malfunction, so this last step was necessary for the circuit to function properly. We used probes connected to micromanipulators to touch down to the pads for outputs and ground. We connected the output of the circuit to the input of an Ithaco 1211 preamplifier and measured the output of the preamplifier

with a digital oscilloscope (Picoscope). For voltage measurements, we put the output of the circuit across a 100-megohm resistor before the input of the preamplifier and calculated the voltage based on the measured current and known resistance. This measurement could also be performed with a high–input impedance oscilloscope without any preamplification, but the input impedance of many standard oscilloscopes is too low (~1 megohm) to give an accurate voltage measurement.

Figure S2 shows measured outputs for the circuit. In fig. S2A, we plot the current versus time for two incident light intensities, 2.5 and 7 kW/m² of a 660-nm light. Figure S2B plots the voltage versus time from two different phase outputs measured simultaneously. Each state output the expected voltage of about ±0.6 V, spanning the oxygen adsorption actuation voltage for SEAs (25). The phase difference matched the expected 90° phase difference for the selected outputs. In fig. S2C, we plot the measured amplitude of the current and the voltage of the square wave outputs from the circuit as a function of light intensity. The current increased with light intensity as expected, yielding a PV responsivity of about 0.3 A/W and an open-circuit voltage of ~0.6 V, typical values for silicon p-n junction PVs of similar thicknesses (41). On the basis of this value and the charge per area for oxygen adsorption actuation of a SEA as measured in previous work (28), about 150 $\mu C/cm^2$, we expected the circuit to be able to drive SEAs with an exposed platinum surface of about 0.1 mm² at 1 Hz at 1 kW/m² of input light intensity, a value more than sufficient for operating the microscopic robots. In fig. S2D, we plot the frequency versus light intensity from one of the circuits, showing an initial linear increase in frequency with light intensity before leveling off after about 2 kW/m². Figure S2E shows current-voltage relation curves for the large PVs for powering the legs of the robot wired in series; the measured voltage and current from the PVs correspond well to the voltage and current delivered from the functioning circuit.

We also perform on-chip testing of the circuit for dogbot. Figure S6A shows an optical image of that circuit before fabrication. To test the circuit electrically, we wired contact pads to the output of the circuit and shielded the circuit from light with a metal layer. In fig. S6B, we show the shift command delivered to the circuit optically. In fig. S6C, we plot the current versus time from the circuit as it received consecutive shift commands. For this experiment, the circuit was powered at about 0.5 kW/m², and the high level for the command was about 3 kW/m². In general, we found that delivering the commands requires a light intensity equal to or greater than 3 kW/m² and that the circuit works best with about 50-μs pulses.

Fabrication process
Because of its length, we provide details of the fabrication process in the Supplementary Materials.

Robot manipulation and operation
To pick up and move individual microscopic robots, we used a pulled micropipette (tip diameter of ~30 μm) attached to a micromanipulator with a custom holder. The micropipette was connected to a syringe pump. We withdrew fluid to attach the robot to the micropipette and pumped out fluid to release. To flip the robots, we attached the same micropipette to a Pneumatic PicoPump (WPI)

and applied a pressure spike to roll the robot over with a small volume of fast-moving water.

To operate the microscopic robots, we simply shone light on them. The robots function in about 0.5 to 5 kW/m² of light, which is comparable with the light intensity outside on a sunny day (about 1 kW/m²). The robots can be operated under any light source that silicon absorbs; in Movie S2, we powered the robot with a halogen lamp. However, for most of the robots, we chose to use light sources at well-known wavelengths to simplify the calibration of light intensity. For the robots in Figs. 3 and 5, we used a 660-nm Thorlabs laser to power the robots and a halogen lamp to image them. For Fig. 4, we used a Thorlabs 600-nm light-emitting diode lamp to both power and image the robot. The robots were exclusively powered and imaged from above. The underside of the circuit for the robot was not shielded from light, so shining light at the bottom of the robot caused the circuit to malfunction and the robot to stop moving.

To give commands to dogbot, we connected a function generator (Agilent 33250A) to the external control input for a Thorlabs laser diode driver. We connected a computer to the function generator and used a home-written python script to deliver commands for an arbitrary square wave, which is output from the function generator to the driver, modulating the laser light intensity.

Estimating the maximum speed of Purcell-bot
In the future, there are several changes to the design of Purcell-bot that we anticipate will allow it to go faster, including increasing the friction between the legs and the surface, increasing the frequency of the motion, and increasing the length of the legs. The following analysis allowed us to estimate the maximum average velocity that a Purcell-bot could achieve with these changes. Actuating a leg of the robot applies a force to the body of the robot equal to the force of friction on the leg, which we will label as leg 1. This force is opposed by the fluid drag on the robot and by the friction on the stationary leg, which we label as leg 2. The maximum speed of the microrobot is set by balancing these forces

$$F_{F1} - F_{F2} - F_d = 0$$

On the basis of balancing forces and torques on Purcell-bot, we expect that the normal force is partitioned between the legs based on their proximity to the center of mass. If we make the simplifying assumption that the coefficient of friction is equal for each leg, we can write the maximum difference between the friction forces as

$$(F_{F1} - F_{F2})_{max} = \eta F_N \frac{d_{leg}}{L_{bot}}$$

where L_{bot} is the separation between the legs when both legs are fully extended, d_{leg} is the displacement of the leg in the x direction, η is the coefficient of friction on the leg, and F_N is the normal force on the robot.

The drag force is made up of contributions from the body and legs of the robot. If we assume that the body of the robot is the dominant contribution to the drag force, we can write

$$F_d \approx \frac{\mu A v}{s}$$

where v is the velocity of the robot, μ is the viscosity of the fluid, A is the area of the robot, and s is the separation between the body of the

robot and the surface (*25*). The maximum velocity of the robot is then about

$$v_{max} = \frac{\eta F_N s}{\mu A} \frac{d_{leg}}{L_{bot}}$$

For the Purcell-bot shown in Fig. 3, d_{leg} is about 10 μm, and L_{bot} is about 150 μm. The circuit at the center of the body of the robot is the dominant contributor to the weight: It is about 60 μm wide, 100 μm long, and 15 μm tall and weighs about 1.5 nN. With a surface area of about 100 μm by 200 μm, a separation distance of about 20 μm based on the length of the legs, the viscosity of water at about 10^{-3} Pa s, and a peak speed of about 50 μm/s, we find a maximum coefficient of friction of about 0.5. The actual value for the coefficient of friction could be lower if the coefficient of friction is different at each of the legs at different times during the gait (i.e., if one leg's friction value is the static coefficient of friction and the other's is the kinetic coefficient of friction) or higher if the drag on the legs contributes substantially to the overall drag. By increasing the friction between the legs and the surface (either by designing a textured surface or engineering the end of the leg) and by redesigning the legs with smaller surface areas to decrease drag forces, we could increase the fraction of the gait where only one leg is sliding on the surface and the other is fixed. This would also increase the maximum speed of the robot, allowing us to increase the frequency of leg motion proportionally to the increased friction. Increasing the length of the legs of the Purcell-bot could further increase the average velocity by increasing both s and d_{leg}. For a robot of the same area and weight on a surface where $\eta \approx 1$, with s and d_{leg} about 50 μm (close to the maximum value because the robots would tip over if they exceed $L_{bot}/2$), we estimate peak velocities of about 1 mm/s and an average velocity of hundreds of micrometers per second, allowing even this simple robot design to travel at body length–per–second speeds. This speed is comparable with or faster than other synthetic microrobots that move near solid surfaces (*12, 25, 57*) but is outpaced by some acoustically or chemically driven systems (*18, 58*).

Estimating efficiency
We can estimate the efficiency of these robots by comparing the incident power on the PVs with the power expended to move the robot's body through the fluid near a surface, given by the drag force on the robot times its velocity

$$P_{drag} = \frac{\mu A v^2}{s}$$

For the Purcell-bot shown in Fig. 4 with an average speed of 4 μm/s, the drag power is about 1 aW. The power incident on the PVs at 1 kW/m² (1 sun) is about 1 μW. This results in an extremely low efficiency of about 10^{-11}.

We can account for this efficiency by considering four "internal efficiencies": the efficiency of the PVs, the power transmission efficiency between the PVs and the SEAs, the SEAs' efficiency, and the efficiency of motion. On the basis of a measured responsivity of 0.3 A/W and an output voltage of about 0.6 V, the PVs have an efficiency of about 20%. The change in voltage output is 1.2 V and 200 nA, values that were designed to overshoot the demanded voltage and

charge for the actuators on the robot, about 0.3 V and about 10 nC. As a result, at a 1-Hz actuation frequency, the power transmission between the PVs and the SEAs is about 1%. The efficiency of the SEAs is about 10^{-4} as measured in previous work (*28*). On the basis of these efficiencies, the efficiency of converting the mechanical work done by the SEAs to forward motion is about 10^{-4}. This includes energy lost to the surrounding fluid, portions of the motion that do not propel the robot forward, and any mismatch between the maximum force output by the actuator and the force generating forward motion. As discussed in the previous section, redesigning the robot's legs, increasing the operating frequency, and increasing friction between the legs and surface could likely yield speeds of around 100 μm/s without increasing the required input power; this could increase the overall efficiency by two to three orders of magnitude. Operating the robots at higher frequencies could also decrease the power consumption of the circuit, requiring fewer frequency divisions, but this improvement would be marginal. For the antbot, which has an area of about 240 μm by 240 μm, moves at 12 μm/s, has an estimated separation from the surface of 25 μm, and is powered by a light intensity of about 4 kW/m² for the data shown in Fig. 4, the estimated efficiency is between 10^{-10} and 10^{-11}, about a factor of 5 greater than for the Purcell-bot in Fig. 3.

Supplementary Materials
This PDF file includes:
Materials and Methods
Figs. S1 to S6

Other Supplementary Material for this manuscript includes the following:
Movies S1 to S3

REFERENCES AND NOTES
1. R. Dreyfus, J. Baudry, M. L. Roper, M. Fermigier, H. A. Stone, J. Bibette, Microscopic artificial swimmers. *Nature* **437**, 862–865 (2005).
2. L. Zhang, J. J. Abbott, L. Dong, B. E. Kratochvil, D. Bell, B. J. Nelson, Artificial bacterial flagella: Fabrication and magnetic control. *Appl. Phys. Lett.* **94**, 064107 (2009).
3. J. Cui, T.-Y. Huang, Z. Luo, P. Testa, H. Gu, X.-Z. Chen, B. J. Nelson, L. J. Heyderman, Nanomagnetic encoding of shape-morphing micromachines. *Nature* **575**, 164–168 (2019).
4. K. E. Peyer, L. Zhang, B. J. Nelson, Bio-inspired magnetic swimming microrobots for biomedical applications. *Nanoscale* **5**, 1259–1272 (2013).
5. J. G. Gibbs, Y.-P. Zhao, Autonomously motile catalytic nanomotors by bubble propulsion. *Appl. Phys. Lett.* **94**, 163104 (2009).
6. W. Gao, A. Uygun, J. Wang, Hydrogen-bubble-propelled zinc-based microrockets in strongly acidic media. *J. Am. Chem. Soc.* **134**, 897–900 (2012).
7. W. Gao, J. Wang, Synthetic micro/nanomotors in drug delivery. *Nanoscale* **6**, 10486–10494 (2014).
8. R. Dong, Y. Cai, Y. Yang, W. Gao, B. Ren, Photocatalytic micro/nanomotors: From construction to applications. *Acc. Chem. Res.* **51**, 1940–1947 (2018).
9. U. M. Córdova-Figueroa, J. F. Brady, Osmotic propulsion: The osmotic motor. *Phys. Rev. Lett.* **100**, 158303 (2008).
10. J. Li, I. Rozen, J. Wang, Rocket science at the nanoscale. *ACS Nano* **10**, 5619–5634 (2016).
11. J. L. Moran, J. D. Posner, Phoretic self-propulsion. *Annu. Rev. Fluid Mech.* **49**, 511–540 (2017).
12. S. Palagi, A. G. Mark, S. Y. Reigh, K. Melde, T. Qiu, H. Zeng, C. Parmeggiani, D. Martella, A. Sanchez-Castillo, N. Kapernaum, F. Giesselmann, D. S. Wiersma, E. Lauga, P. Fischer, Structured light enables biomimetic swimming and versatile locomotion of photoresponsive soft microrobots. *Nat. Mater.* **15**, 647–653 (2016).
13. C. Xin, D. Jin, Y. Hu, L. Yang, R. Li, L. Wang, Z. Ren, D. Wang, S. Ji, K. Hu, D. Pan, H. Wu, W. Zhu, Z. Shen, Y. Wang, J. Li, L. Zhang, D. Wu, J. Chu, Environmentally adaptive shape-morphing microrobots for localized cancer cell treatment. *ACS Nano* **15**, 18048–18059 (2021).

14. V. K. Bandari, Y. Nan, D. Karnaushenko, Y. Hong, B. Sun, F. Striggow, D. D. Karnaushenko, C. Becker, M. Faghih, M. Medina-Sánchez, F. Zhu, O. G. Schmidt, A flexible microsystem capable of controlled motion and actuation by wireless power transfer. *Nat. Electron.* **3**, 172–180 (2020).

15. B. J. Williams, S. V. Anand, J. Rajagopalan, M. T. A. Saif, A self-propelled biohybrid swimmer at low Reynolds number. *Nat. Commun.* **5**, 3081 (2014).

16. L. Ricotti, B. Trimmer, A. W. Feinberg, R. Raman, K. K. Parker, R. Bashir, M. Sitti, S. Martel, P. Dario, A. Menciassi, Biohybrid actuators for robotics: A review of devices actuated by living cells. *Sci. Robot.* **2**, eaaq0495 (2017).

17. K. J. Rao, F. Li, L. Meng, H. Zheng, F. Cai, W. Wang, A force to be reckoned with: A review of synthetic microswimmers powered by ultrasound. *Small* **11**, 2836–2846 (2015).

18. L. Ren, N. Nama, J. M. McNeill, F. Soto, Z. Yan, W. Liu, W. Wang, J. Wang, T. E. Mallouk, 3D steerable, acoustically powered microswimmers for single-particle manipulation. *Sci. Adv.* **5**, eaax3084 (2019).

19. B. Dai, J. Wang, Z. Xiong, X. Zhan, W. Dai, C.-C. Li, S.-P. Feng, J. Tang, Programmable artificial phototactic microswimmer. *Nat. Nanotechnol.* **11**, 1087–1092 (2016).

20. C. Lozano, B. ten Hagen, H. Löwen, C. Bechinger, Phototaxis of synthetic microswimmers in optical landscapes. *Nat. Commun.* **7**, 12828 (2016).

21. M. Ibele, T. E. Mallouk, A. Sen, Schooling behavior of light-powered autonomous micro-motors in water. *Angew. Chem. Int. Ed.* **48**, 3308–3312 (2009).

22. Y. Hong, N. M. K. Blackman, N. D. Kopp, A. Sen, D. Velegol, Chemotaxis of nonbiological colloidal rods. *Phys. Rev. Lett.* **99**, 178103 (2007).

23. C. Jin, C. Krüger, C. C. Maass, Chemotaxis and autochemotaxis of self-propelling droplet swimmers. *Proc. Natl. Acad. Sci.* **114**, 5089–5094 (2017).

24. W. Gao, X. Feng, A. Pei, Y. Gu, J. Li, J. Wang, Seawater-driven magnesium based Janus mi-cromotors for environmental remediation. *Nanoscale* **5**, 4696–4700 (2013).

25. M. Z. Miskin, A. J. Cortese, K. Dorsey, E. P. Esposito, M. F. Reynolds, Q. Liu, M. Cao, D. A. Muller, P. L. McEuen, I. Cohen, Electronically integrated, mass-manufactured, micro-scopic robots. *Nature* **584**, 557–561 (2020).

26. W. Hu, G. Z. Lum, M. Mastrangeli, M. Sitti, Small-scale soft-bodied robot with multimodal locomotion. *Nature* **554**, 81–85 (2018).

27. T. Xu, J. Zhang, M. Salehizadeh, O. Onaizah, E. Diller, Millimeter-scale flexible robots with programmable three-dimensional magnetization and motions. *Sci. Robot.* **4**, eaav4494 (2019).

28. A. M. Brooks, M. S. Strano, A conceptual advance that gives microrobots legs. *Nature* **584**, 530–531 (2020).

29. R. S. Pierre, S. Bergbreiter, Toward autonomy in sub-gram terrestrial robots. *Annu. Rev. Control Robot. Autonom. Syst.* **2**, 231–252 (2019).

30. V. K. Bandari, O. G. Schmidt, System-engineered miniaturized robots: From structure to intelligence. *Adv. Intell. Syst.* **3**, 2000284 (2021).

31. S. Palagi, P. Fischer, Bioinspired microrobots. *Nat. Rev. Mater.* **3**, 113–124 (2018).

32. T.-Y. Huang, H. Gu, B. J. Nelson, Increasingly intelligent micromachines. *Rev. Control Robot. Autonom. Syst.* **5**, 279–310 (2022).

33. A. C. Molnar, S. Lee, A. Cortese, P. McEuen, S. Sadeghi, S. Ghajari, Nanoliter-scale autono-mous electronics: Advances, challenges, and opportunities, in *2021 IEEE Custom Integrated Circuits Conference (CICC)* (IEEE, 2021), pp. 1–6.

34. S. Hollar, A. Flynn, C. Bellew, K. S. J. Pister, Solar powered 10 mg silicon robot, in *IEEE The Sixteenth Annual International Conference on Micro Electro Mechanical Systems, 2003. MEMS-03 Kyoto* (2003), pp. 706–711.

35. R. Yeh, K. S. J. Pister, Design of low-power silicon articulated microrobots. *J. Micromecha-tron.* **1**, 9 (2001).

36. W. A. Churaman, L. J. Currano, C. J. Morris, J. E. Rajkowski, S. Bergbreiter, The first launch of an autonomous thrust-driven microrobot using nanoporous energetic silicon. *J. Microelectromech. Syst.* **21**, 198–205 (2012).

37. K. Saito, K. Sugita, Y. Ishihara, K. Iwata, Y. Asano, Y. Okane, S. Ono, S. Chiba, M. Takato, F. Uchikoba, Insect-type MEMS microrobot with mountable bare chip IC of artificial neural networks. *Artif. Life Robot.* **22**, 118–124 (2017).

38. Q. Liu, W. Wang, M. F. Reynolds, M. C. Cao, M. Z. Miskin, T. A. Arias, D. A. Muller, P. L. McEuen, I. Cohen, Micrometer-sized electrically programmable shape-memory actuators for low-power microrobotics. *Sci. Robot.* **6**, eabe6663 (2021).

39. S. Lee, A. J. Cortese, A. P. Gandhi, E. R. Agger, P. L. McEuen, A. C. Molnar, A 250 μm × 57 μm microscale opto-electronically transduced electrodes (MOTEs) for neural recording. *IEEE Trans. Biomed. Circuits Syst.* **12**, 1256–1266 (2018).

40. S. Lee, A. J. Cortese, A. Mok, C. Wu, T. Wang, J. U. Park, C. Smart, S. Ghajari, D. Khilwani, S. Sadeghi, Y. Ji, J. H. Goldberg, C. Xu, P. L. McEuen, A. C. Molnar, Fabrication of injectable micro-scale opto- electronically transduced electrodes (MOTEs) for physiological moni-toring. *J. Microelectromech. Syst.* **29**, 720–726 (2020).

41. A. J. Cortese, C. L. Smart, T. Wang, M. F. Reynolds, S. L. Norris, Y. Ji, S. Lee, A. Mok, C. Wu, F. Xia, N. I. Ellis, A. C. Molnar, C. Xu, P. L. McEuen, Microscopic sensors using optical wireless in-tegrated circuits. *Proc. Natl. Acad. Sci. U.S.A.* **117**, 9173–9179 (2020).

42. E. M. Purcell, Life at low Reynolds number. *Am. J. Phys.* **45**, 3–11 (1977).

43. D. M. Wilson, Insect walking. *Annu. Rev. Entomol.* **11**, 103–122 (1966).

44. P. Ramdya, R. Thandiackal, R. Cherney, T. Asselborn, R. Benton, A. J. Ijspeert, D. Floreano, Climbing favours the tripod gait over alternative faster insect gaits. *Nat. Commun.* **8**, 14494 (2017).

45. B. S. Leibowitz, B. E. Boser, K. S. J. Pister, in *Sensors and Camera Systems for Scientific, In-dustrial, and Digital Photography Applications II* (SPIE, 2001), vol. 4306, pp. 308–318; https://spiedigitallibrary.org/conference-proceedings-of-spie/4306/0000/CMOS-smart-pixel-for-free-space-optical-communication/10.1117/12.426966.full.

46. B. S. Leibowitz, B. E. Boser, K. S. J. Pister, A 256-element CMOS imaging receiver for free-space optical communication. *IEEE J. Solid State Circuits* **40**, 1948–1956 (2005).

47. A. von Rohr, S. Trimpe, A. Marco, P. Fischer, S. Palagi, Gait learning for soft microrobots controlled by light fields, in *Proceedings of the 2018 IEEE/RSJ International Conference on Intelligent Robots and Systems (IROS)* (IEEE, 2018), pp. 6199–6206.

48. F. Alouges, A. D. Simone, L. Giraldi, Y. Or, O. Wiezel, Energy-optimal strokes for multi-link microswimmers: Purcell's loops and Taylor's waves reconciled. *New J. Phys.* **21**, 043050 (2019).

49. D. Tam, A. E. Hosoi, Optimal stroke patterns for Purcell's three-link swimmer. *Phys. Rev. Lett.* **98**, 068105 (2007).

50. S. Ramasamy, R. L. Hatton, Optimal gaits for drag-dominated swimmers with passive elastic joints. *Phys. Rev. E.* **103**, 032605 (2021).

51. L. Soler, V. Magdanz, V. M. Fomin, S. Sanchez, O. G. Schmidt, Self-propelled micromotors for cleaning polluted water. *ACS Nano* **7**, 9611–9620 (2013).

52. M. Hempel, V. Schroeder, C. Park, V. B. Koman, M. Xue, E. McVay, S. Spector, M. Dubey, M. S. Strano, J. Park, J. Kong, T. Palacios, SynCells: A 60 × 60 μm² electronic platform with remote actuation for sensing applications in constrained environments. *ACS Nano* **15**, 8803–8812 (2021).

53. R. Fernandes, D. H. Gracias, Self-folding polymeric containers for encapsulation and de-livery of drugs. *Adv. Drug Deliv. Rev.* **64**, 1579–1589 (2012).

54. W. Gao, D. Kagan, O. S. Pak, C. Clawson, S. Campuzano, E. Chuluun-Erdene, E. Shipton, E. E. Fullerton, L. Zhang, E. Lauga, J. Wang, Cargo-towing fuel-free magnetic nano-swimmers for targeted drug delivery. *Small* **8**, 460–467 (2012).

55. M. Sitti, H. Ceylan, W. Hu, J. Giltinan, M. Turan, S. Yim, E. Diller, Biomedical applications of untethered mobile milli/microrobots. *Proc. IEEE* **103**, 205–224 (2015).

56. H. Suzuki, R. J. Wood, Origami-inspired miniature manipulator for teleoperated microsur-gery. *Nat. Mach. Intell.* **2**, 437–446 (2020).

57. H. Zeng, P. Wasylczyk, C. Parmeggiani, D. Martella, M. Burresi, D. S. Wiersma, Light-fueled microscopic walkers. *Adv. Mater.* **27**, 3883–3887 (2015).

58. H. Wang, J. G. S. Moo, M. Pumera, From nanomotors to micromotors: The influence of the size of an autonomous bubble-propelled device upon its motion. *ACS Nano* **10**, 5041–5050 (2016).